Size and host-medium effects on topologically protected surface states in bianisotropic three-dimensional optical waveguides

Vasily V. Klimov,[1,2,3,*] Dmitry V. Guzatov,[4] Ilya V. Zabkov,[1,2] Hsun-Chi Chan,[5] and Guang-Yu Guo[5,6,†]

[1]*Dukhov Research Institute of Automatics (VNIIA), 22, Sushchevskaya str., 127055, Moscow, Russia*
[2]*P.N. Lebedev Physical Institute, Russian Academy of Sciences, Leninsky Prospekt. 53, 119991, Moscow, Russia*
[3]*National Research Nuclear University MEPhI, Kashirskoe shosse 31, 115409, Moscow, Russia*
[4]*Yanka Kupala State University of Grodno, 22 Ozheshko street, 230023, Grodno, Belarus*
[5]*Department of Physics and Center for Theoretical Physics, National Taiwan University, Taipei 10617, Taiwan*
[6]*Physics Division, National Center for Theoretical Sciences, Hsinchu 30013, Taiwan*

We study the optical properties of bianisotropic optical waveguides with nontrivial topological structure in wave-vector space, placed in an ordinary dielectric matrix. We derive an exact analytical description of the eigenmodes of the systems with arbitrary parameters that allows us to investigate topologically protected surface states (TPSS) in details. In particular, we find that the TPSS in the waveguides would disappear (1) if their radius is smaller than a critical value due to the dimensional quantization of azimuthal wave number, and also (2) if the permittivity of the host medium exceeds a critical value. Interestingly, we discover that the TPSS in the waveguides have negative refraction for some structures. We construct a TPSS phase diagram that will guide the development of topological waveguides for optical interconnects and devices.

I. INTRODUCTION

Electronic properties of topological phases of matter, including topological insulators, have been under intensive investigation in the past decades [1–4]. This culminated in the Nobel Prize in Physics in 2016 being awarded to D. J. Thouless, F. D. M. Haldane, and J. M. Kosterlitz "for theoretical discoveries of topological phase transitions and topological phases of matter" [5]. In the meantime, this intensive interest in topological phases of matter has also stimulated widespread studies on complex topology of dispersion relations of photonic crystals and metamaterials, leading to the appearance of topological photonics [6–19], a new and vibrant area in nanophotonics and nano-optics. Examples of such photonic materials include bianisotropic materials [7,8], magnetized cold plasma [9,10], or planar photonic crystals [11–15]. The nontrivial topology in wave-vector space can be observed also in ferrite films [20,21]. Several experimental works of this kind are known both in microwaves [16,17] and in optics [18,19].

Among other things, the most interesting effect here is topologically protected surface states (TPSS), whose one-way propagation should be insensitive to the spatial variations of the waveguide surface. These states are often considered as the analogs of conducting surface states in electronic topological insulators [4]. However, there are some fundamental differences between the surface states in electronic and photonic topological insulators. First, electrons have a mass and a charge and cannot disappear. Second, electrons are subject to Fermi-Dirac statistics, whereas photons are subject to Bose-Einstein statistics. The third and most important difference is that the extension of electronic wave function is generally much smaller than the system size, and therefore the systems can be considered as infinite half spaces. On the other hand, the wavelengths of photons in the visible regime, for example, are on the order of 1 μm, and thus can be larger than the transverse size of the optical system, especially optical nanowaveguides. These differences can render the concept of TPSS in photonics invalid in certain circumstances. Furthermore, two-dimensional (2D) propagation of TPSS in a flat interfacial plane or on a flat surface is usually considered in topological photonics. However, one major goal of the topological photonics is the design of long three-dimensional nanowaveguides with small losses which can be used as optical interconnects [22,23].

To meet this goal, in this paper we present the results of our detailed study of the fundamental properties of TPSS in waveguides of realistic geometries made of photonic metamaterials. Main attention is paid to the investigation of how the waveguide geometry influences its properties and even the existence of TPSS. In doing so we will consider waveguides of different radius and different cross sections (see Fig. 1). We will also consider how the properties of environment affect the TPSS. In particular, we derive an analytical solution for the considered system. Based on this analytical solution, we thoroughly investigate the optical properties, especially those which have been overlooked so far, of the TPSS, such as the limited validity of the TPSS concept.

By ways of example, we focus on the nanowaveguides made of a bianisotropic material with constitutive relations [24]:

$$\mathbf{D} = \hat{\varepsilon}\mathbf{E} - i\chi\mathbf{H}, \quad \mathbf{B} = \mu\mathbf{H} + i\chi\mathbf{E}. \tag{1}$$

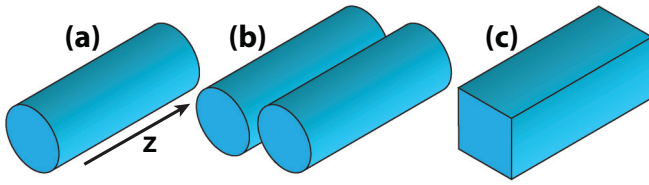*klimov256@gmail.com
†gyguo@phys.ntu.edu.tw

FIG. 1. Geometries under consideration. (a) Single-wire waveguide, (b) two-wire waveguide, and (c) single square waveguide. All waveguides are made of a bianisotropic material with nontrivial topology in wave-vector space, while host medium is an ordinary dielectric.

The permittivity tensor $\hat{\varepsilon}$ in (1) has the following form:

$$\hat{\varepsilon} = \begin{pmatrix} \varepsilon_\rho & 0 & 0 \\ 0 & \varepsilon_\rho & 0 \\ 0 & 0 & \varepsilon_z \end{pmatrix}, \tag{2}$$

where $\varepsilon_\rho = \varepsilon_x = \varepsilon_y$ are the components of the permittivity tensor along Cartesian axes x and y, and ε_z is the permittivity component along Cartesian axis z. Let the medium under consideration have isotropic magnetic permeability μ and isotropic chirality parameter χ. We also assume that the waveguide is placed in ordinary isotropic dielectric host of permittivity ε_d. When $\varepsilon_\rho > 0$ and $\varepsilon_z < 0$ (hyperbolic case [25]) such medium has nontrivial topology in reciprocal space. It is important to note that Eqs. (1) and (2) do not violate time-reversal symmetry as was previously shown in Ref. [7]. Another remarkable feature of Eqs. (1) and (2) is that there is no leaking of electromagnetic waves to vacuum in the case of arbitrary interface between vacuum and chiral hyperbolic half spaces [7].

This paper is organized as follows. The derived analytical expression for the dispersion relations for the cylindrical waveguide is presented in Sec. II. Section III is devoted to the study of the topology of the surfaces defined by dispersion relations of bulk bianisotropic media and associated singularity of wave vectors. Here we have calculated Chern numbers of all bands also. The influence of the waveguide radius R on the TPSS is analyzed in Sec. IV. In particular, it is shown in

this section that there is a critical radius R_c below which the TPSS would disappear due to the dimensional quantization of eigenmodes. The optical properties of TPSS of a two-wire system are analyzed in Sec. V. The influence of cross-section shape on TPSS is analyzed in Sec. VI. The effect of permittivity ε_d of surrounding medium on TPSS is studied in Sec. VII. Changes in the dispersion relations of the interface due to the ε_d variation are reported. In particular, it is demonstrated that for a large enough ε_d, TPSS would also disappear. In Sec. VIII the calculated group velocity of TPSS is reported to show that for certain sets of R and ε_d values, the group velocity is opposite to the phase velocity, resulting in a negative refractive index. In Sec. IX a generalized phase diagram of TPSS in cylindrical bianisotropic waveguides is presented and the conclusions drawn from this work are also given.

II. ELECTROMAGNETIC WAVES IN A CYLINDRICAL BIANISOTROPIC WAVEGUIDE: AN ANALYTIC SOLUTION

To find general expressions of fields inside the bianisotropic metamaterial waveguide with translational symmetry along the z axis, one can integrate over longitudinal wave vector h. In this way, general expressions have the following form:

$$\mathbf{E}^{\text{in}} = \int_{-\infty}^{\infty} dh \mathbf{E}, \quad \mathbf{H}^{\text{in}} = \int_{-\infty}^{\infty} dh \mathbf{H}. \tag{3}$$

In the case of a circular cylindrical waveguide made of a bianisotropic metamaterial (1) one can solve wave equations in the cylindrical system of coordinates $0 < \rho < \infty$, $0 \leqslant \varphi < 2\pi$ and $-\infty < z < \infty$. In this case, we can show that z components of the fields can be written as

$$E_z = \sum_{n=-\infty}^{\infty} \left(B_n^P J_n(q_P \rho) + B_n^M J_n(q_M \rho) \right) e^{ihz+in\varphi}$$

$$H_z = \sum_{n=-\infty}^{\infty} \left(f B_n^P J_n(q_P \rho) + g B_n^M J_n(q_M \rho) \right) e^{ihz+in\varphi}, \tag{4}$$

where $J_n(x)$ is the Bessel function [26], B_n^P and B_n^M are coefficients which we can find from the boundary conditions, and q_P, q_M are radial wave vectors:

$$q_{\binom{P}{M}} = \sqrt{\left(k_0^2 - \frac{h^2}{\varepsilon_\rho \mu - \chi^2} \right) \left(\frac{(\varepsilon_\rho + \varepsilon_z)\mu}{2} - \chi^2 \right) + 2k_0^2 \chi (\chi \mp b\mu)}$$

$$a = \frac{\varepsilon_\rho - \varepsilon_z}{4k_0^2 \chi} \left(k_0^2 - \frac{h^2}{\varepsilon_\rho \mu - \chi^2} \right), \quad b = \sqrt{\frac{\varepsilon_z}{\mu} + a\left(a + \frac{2\chi}{\mu} \right)}. \tag{5}$$

Equations (4) and (5) allow us to find an analytical solution of the problem. The other field components in the matrix form are given as follows:

$$\begin{pmatrix} E_\rho \\ H_\rho \end{pmatrix} = \frac{ih}{A} M_1 \frac{\partial}{\partial \rho} \begin{pmatrix} E_z \\ H_z \end{pmatrix} - \frac{ik_0}{A} M_2 \frac{1}{\rho} \frac{\partial}{\partial \varphi} \begin{pmatrix} -H_z \\ E_z \end{pmatrix}$$

$$\begin{pmatrix} E_\varphi \\ H_\varphi \end{pmatrix} = \frac{ih}{A} M_1 \frac{1}{\rho} \frac{\partial}{\partial \varphi} \begin{pmatrix} E_z \\ H_z \end{pmatrix} + \frac{ik_0}{A} M_2 \frac{\partial}{\partial \rho} \begin{pmatrix} -H_z \\ E_z \end{pmatrix}, \tag{6}$$

where

$$
\begin{aligned}
M_1 &= \begin{pmatrix} k_0^2(\varepsilon_\rho\mu + \chi^2) - h^2 & 2ik_0^2\mu\chi \\ -2ik_0^2\varepsilon_\rho\chi & k_0^2(\varepsilon_\rho\mu + \chi^2) - h^2 \end{pmatrix} \\
M_2 &= \begin{pmatrix} \mu\big(k_0^2(\varepsilon_\rho\mu - \chi^2) - h^2\big) & i\chi\big(k_0^2(\varepsilon_\rho\mu - \chi^2) + h^2\big) \\ -i\chi\big(k_0^2(\varepsilon_\rho\mu - \chi^2) + h^2\big) & \varepsilon_\rho\big(k_0^2(\varepsilon_\rho\mu - \chi^2) - h^2\big) \end{pmatrix} \\
A &= \big(k_0^2(\sqrt{\varepsilon_\rho\mu} - \chi)^2 - h^2\big)\big(k_0^2(\sqrt{\varepsilon_\rho\mu} + \chi)^2 - h^2\big).
\end{aligned}
\tag{7}
$$

General expressions for the fields outside the waveguide in an ordinary dielectric medium of permittivity ε_d and permeability being equal to unit can be written in a similar way

$$
\mathbf{E}^{\text{out}} = \int_{-\infty}^{\infty} dh\,\mathbf{E}', \quad \mathbf{H}^{\text{out}} = \int_{-\infty}^{\infty} dh\,\mathbf{H}',
\tag{8}
$$

$$
E_z' = \sum_{n=-\infty}^{\infty} C_n H_n^{(1)}(q\rho)e^{ihz+in\varphi}, \quad H_z' = \sum_{n=-\infty}^{\infty} D_n H_n^{(1)}(q\rho)e^{ihz+in\varphi},
$$

$$
\begin{pmatrix} E_\rho' \\ H_\rho' \end{pmatrix} = \frac{ih}{q^2}\frac{\partial}{\partial\rho}\begin{pmatrix} E_z' \\ H_z' \end{pmatrix} - \frac{ik_0}{q^2}\frac{1}{\rho}\frac{\partial}{\partial\varphi}\begin{pmatrix} -H_z' \\ \varepsilon_d E_z' \end{pmatrix}, \quad \begin{pmatrix} E_\varphi' \\ H_\varphi' \end{pmatrix} = \frac{ih}{q^2}\frac{1}{\rho}\frac{\partial}{\partial\varphi}\begin{pmatrix} E_z' \\ H_z' \end{pmatrix} + \frac{ik_0}{q^2}\frac{\partial}{\partial\rho}\begin{pmatrix} -H_z' \\ \varepsilon_d E_z' \end{pmatrix},
\tag{9}
$$

where $H_n^{(1)}(x)$ is the Hankel function of the first kind [26], $q = \sqrt{k_0^2\varepsilon_d - h^2}$, and coefficients C_n and D_n can be found from the boundary conditions.

The nontrivial solution of the system of equations at the boundary is possible only when determinant D of the system is equal to zero. This then leads to the dispersion equation:

$$
\begin{aligned}
D = & \left\{\frac{nh}{R}\left[\sigma(1,-1) + 2ik_0^2\mu\chi f - \frac{A}{q^2}\right] + ik_0 q_P\left[[\mu f\sigma(-1,-1) - i\chi\sigma(-1,1)]\xi_n(q_P R) - \frac{f\psi_n}{q_P}\right]\right\} \\
& \times \left\{-\frac{nh}{R}\left[g\sigma(1,-1) - 2ik_0^2\varepsilon_\rho\chi - \frac{gA}{q^2}\right] + ik_0 q_M\left[[\varepsilon_\rho\sigma(-1,-1) + i\chi g\sigma(-1,1)]\xi_n(q_M R) - \frac{\varepsilon_d\psi_n}{q_M}\right]\right\} \\
& - \left\{\frac{nh}{R}\left[\sigma(1,-1) + 2ik_0^2\mu\chi g - \frac{A}{q^2}\right] + ik_0 q_M\left[[\mu g\sigma(-1,-1) - i\chi\sigma(-1,1)]\xi_n(q_M R) - \frac{g\psi_n}{q_M}\right]\right\} \\
& \times \left\{-\frac{nh}{R}\left[f\sigma(1,-1) - 2ik_0^2\varepsilon_\rho\chi - \frac{fA}{q^2}\right] + ik_0 q_P\left[[\varepsilon_\rho\sigma(-1,-1) + i\chi f\sigma(-1,1)]\xi_n(q_P R) - \frac{\varepsilon_d\psi_n}{q_P}\right]\right\} = 0, \quad (10)
\end{aligned}
$$

where

$$
\xi_n(x) = \frac{J_n'(x)}{J_n(x)}, \quad \psi_n = \frac{A}{q}\frac{H_n^{(1)\prime}(qR)}{H_n^{(1)}(qR)}
$$

$$
\sigma(s_1, s_2) = k_0^2(\varepsilon_\rho\mu + s_1\chi^2) + s_2 h^2.
\tag{11}
$$

In the special case of $\chi \to 0$ and $\varepsilon_\rho = \varepsilon_z = \varepsilon$, Eq. (10) correctly reduces to the dispersion equation of a waveguide made of an ordinary material [27]. Equations (4)–(11) are the main result of this work and they allow us to investigate all surface and bulk states in details.

III. PROPERTIES AND SINGULAR POINTS OF BULK BIANISOTROPIC MATERIAL

A band structure $\omega = \omega(k_x, h)$ of a spatially homogeneous bianisotropic material can be found with help of the theory of uniaxial bianisotropic media [28]. For a material with

constitutive relations (1) and (2), this equation is

$$
\begin{aligned}
&\left(\frac{h^2}{(\varepsilon_\rho\mu - \chi^2)} + \frac{k_x^2}{(\varepsilon_z\mu - \chi^2)} - \frac{\omega^2}{c^2}\right) \\
&\quad \times \left(\frac{h^2\varepsilon_\rho}{(\varepsilon_\rho\mu - \chi^2)} + \frac{k_x^2\varepsilon_z}{(\varepsilon_z\mu - \chi^2)} - \varepsilon_\rho\frac{\omega^2}{c^2}\right) \\
&= \frac{\chi^2}{\mu}\left(\frac{h^2}{(\varepsilon_\rho\mu - \chi^2)} + \frac{k_x^2}{(\varepsilon_z\mu - \chi^2)} + \frac{\omega^2}{c^2}\right)^2, \quad (12)
\end{aligned}
$$

where k_x and h are, respectively, the x- and z components of the wave vector, and c the speed of light. Without loss of generality, we set $k_y = 0$ for simplicity. This band structure is shown in Fig. 2, and is also plotted in Fig. 3 for a fixed frequency $\omega = k_0 c$ (the red curve in Fig. 2).

Figure 2 shows clearly that the band structure consists of three sheets (bands), namely, one closed surface centered at Γ and the two other open surfaces situated above and below (in the h direction) this closed surface. These three bands are separated by two gaps. Interestingly, all three bands are topologically nontrivial because they all have a
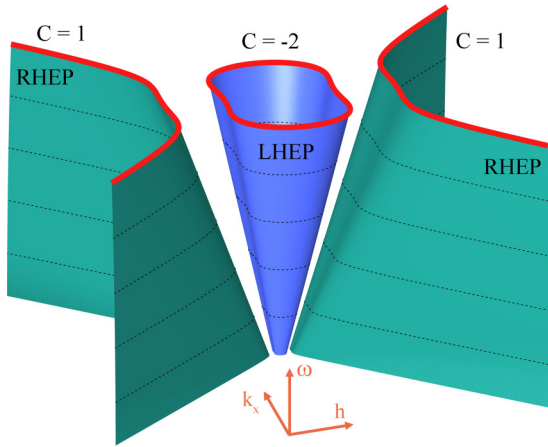
FIG. 2. Band structure $\omega = \omega(k_x, h)$ of a bulk bianisotropic material [Eq. (12)]. Here $\varepsilon_\rho = 4$, $\varepsilon_z = -3$, $\mu = 0.5$, and $\chi = 0.5$. Calculated Chern numbers of the surfaces are labeled on the top. The red curve on the top is the equifrequency curve plotted again in Fig. 3 below. LHEP and RHEP stand for left- and right-handed elliptical polarizations of eigenmodes, correspondingly.

FIG. 4. Schematic presentation of the zones of longitudinal wave vector h (numbers to the left) for which radial wave vectors q_P and q_M are either real, imaginary, or complex. Black lines denote the equifrequency curves of the bulk bianisotropic material. The band Chern numbers (1 and -2) are shown as well. The hatched area corresponds to possible TPSS.

nonzero Chern number**,** as indicated in Fig. 2. Calculation of Chern invariants for continuous media is not a trivial task [29,30]. Here the Berry curvature and the Chern numbers are calculated by using the efficient numerical algorithm reported in Ref. [31] (see also Ref. [15] for more details) and our calculated Chern numbers agree with those reported in Ref. [7]. It should be pointed out that the Chern number *usually* vanishes in most time-reversal-invariant (TRI) systems especially in electronic topological insulators. However, in 2D TRI topological insulators, the Chern numbers for spin-up and spin-down band structures are separately nonzero, but they have equal sizes and opposite signs, thus resulting in zero total Chern number. Nonetheless, even in this case, if one could introduce a TRI symmetry breaking (e.g., spatial asymmetry) that would be sufficiently strong so that a band gap separating spin-up and spin-down bands were opened, one could have a TRI topological insulator with a nonzero Chern number. Unfortunately, no such symmetry breaking has been found so far in the electronic TRI topological insulators. Excitingly,
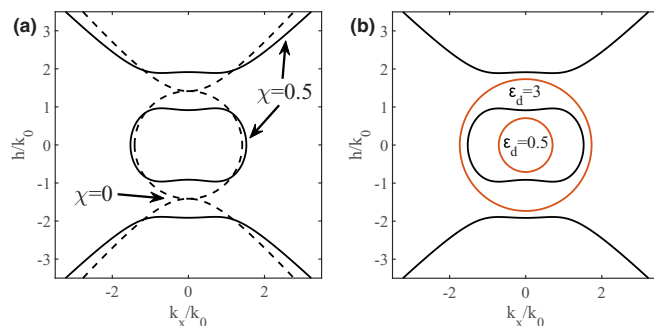

FIG. 3. (a) Equifrequency curves in a bulk bianisotropic material ($\varepsilon_\rho = 4$, $\varepsilon_z = -3$, $\mu = 0.5$) with $\chi = 0$ (dashed lines) and $\chi = 0.5$ (solid lines). (b) Equifrequency lines for an ordinary bulk dielectric with $\varepsilon_d = 0.5$ and $\varepsilon_d = 3$ (red lines). Black lines are the same as in (a).
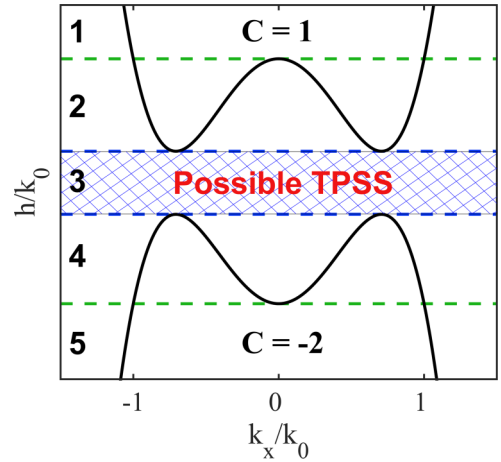
this has recently been shown to be possible in photonic TRI topological insulators with pseudospins by Gao *et al.* [7]. Here pseudospin-up and pseudospin-down are mimicked by two circularly polarized states (or equivalently, TE and TM modes). When the isotropic chirality (i.e., χ becomes nonzero) is introduced, the two pseudospin bands split with equal and opposite Chern numbers [see Fig. 1(c) in Ref. [7] and also Fig. 3(a)]. As hyperbolicity is further introduced, the outer chiral band becomes separated into two bands, resulting in two nontrivial band gaps [see Fig. 1(f) in Ref. [7] and also Fig. 2]. The lower band gap has a gap Chern number of $+1$ while the upper band gap has a gap Chern number of -1 (Fig. 1(f) in Ref. [7]). Therefore, chiral hyperbolic metamaterials are a rare family of topological insulators with TRI yet having a nonzero Chern number. Another type of TRI system in photonics which is based on bianisotropic photonic crystals is presented in Ref. [8]. Note that the gaps would open only when all components of chirality tensor become nonzero. For example, the simple uniaxial chirality $\chi_x = \chi_y = 0$, $\chi_z \neq 0$ would not open a gap in wave-vector space [32].

It is important to note that the equifrequency curve of an ordinary bulk material such as the host dielectric for our waveguide can lie either inside or outside the equifrequency curves of the bianisotropic material or even cross them depending on ε_d. This is demonstrated in Fig. 3(b). As a result, the properties of TPSS can be significantly affected by the host-dielectric and this will be discussed in Sec. VII below.

Before analyzing modes of the bianisotropic waveguide [solution of Eq. (10)], one should consider radial wave vectors q_P and q_M [see Eq. (5)], because they will define the type of the modes of the cylinder. They could be either imaginary, real, or complex, depending on longitudinal wave vector h. The h values for which wave vectors q_P and q_M change their behavior are shown as blue and green lines in Fig. 4.

There are five zones which are separated by the dashed green and blue lines. For h/k_0 in zones 1 and 5, wave vector q_P is
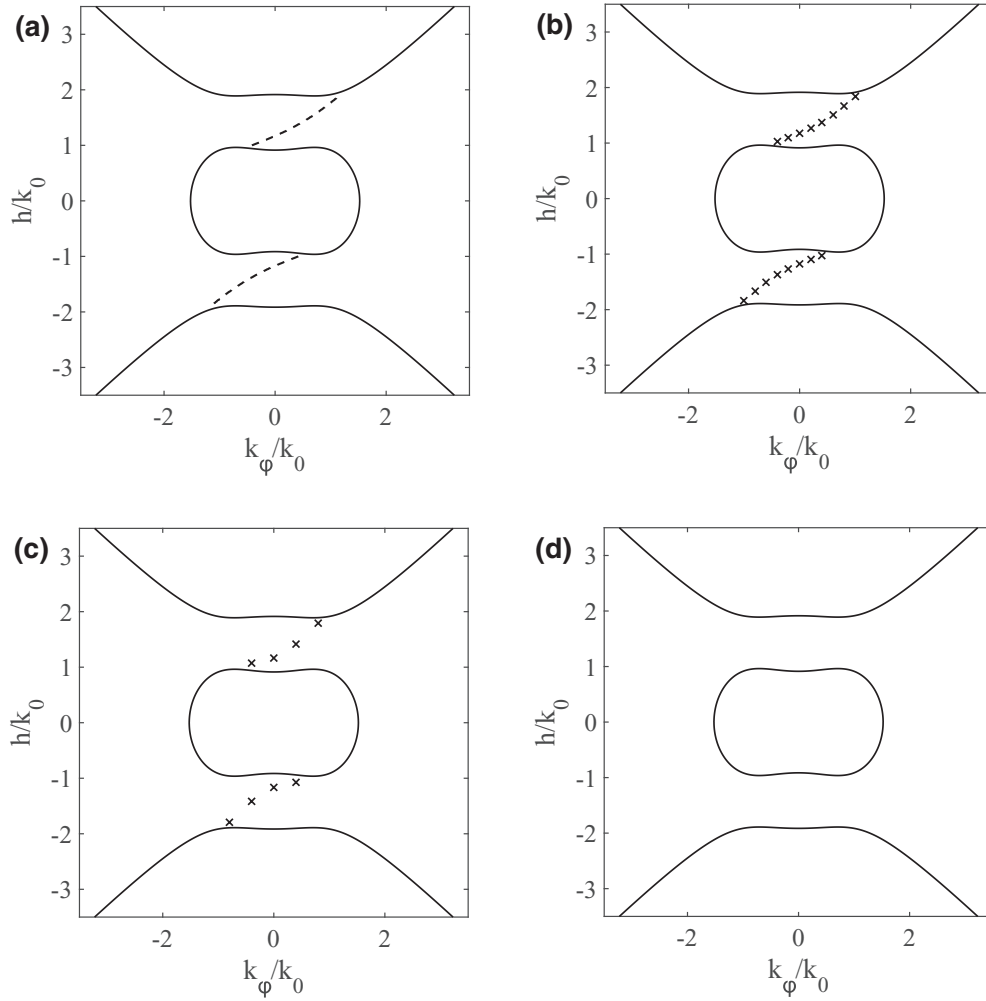
FIG. 5. Eigenvalues of the bianisotropic waveguide with different $k_0 R$ values (dashed curves and crosses) together with equifrequency curves of the bulk bianisotropic material [Eq. (12)] (solid lines). (a) Planar interface $k_0 R \to \infty$, (b) $k_0 R = 5$, (c) $k_0 R = 2.5$, and (d) $k_0 R = 0.5$. Note that when $k_0 R = 0.5$ (d) or smaller, there are no TPSS at all.

imaginary while q_M is real. For h/k_0 in zones 2 and 4, q_P and q_M are real. For h/k_0 in zone 3, q_P and q_M are complex. As a result, bulk modes in the waveguide can in principle appear in zones 1, 2, 4, and 5. Therefore, the only zone where TPSS can exist is zone 3. Note that for a negative χ value, wave vectors q_M and q_P swap places.

IV. INFLUENCE OF THE WAVEGUIDE RADIUS ON TPSS PROPERTIES

It is well known from the theory of usual optical waveguides [33] that for a given frequency, most of the eigenmodes would eventually disappear with decreasing waveguide radius. In this section, let us perform an analogous study on topologically protected surface waves in a circular waveguide made of the bianisotropic metamaterial which reveals that TPSS would indeed disappear when its radius becomes sufficiently small.

In order to link the modes in the entire space (Fig. 3) to that of the waveguide, here we introduce the azimuthal wave vector k_φ:

$$k_\varphi = n/R, \tag{13}$$

where R is the radius of the waveguide. For a planar interface, $k_\varphi \to k_x$. In Fig. 5, solutions of Eq. (10) as a function of h/k_0 and $k_\varphi/k_0 = n/(k_0 R)$ for different $k_0 R$ values are shown as black crosses. Here we consider the waveguide with the same parameters $\varepsilon_\rho = 4$, $\varepsilon_z = -3$, $\mu = 0.5$, and $\chi = 0.5$ as those considered in Ref. [7] for the convenience of comparison. The bands of the bulk bianisotropic material are shown again as solid lines.

It is clear that for the bianisotropic material filling the half space, there are topologically protected modes connecting bands of different Chern numbers. This corresponds to the waveguide with an infinite radius $k_0 R \to \infty$ [see Fig. 5(a)]. Thus, our results are in good agreement with the result reported in Ref. [7]. Similar solutions exist for the waveguide with a finite radius. However, since the cross section of the bianisotropic waveguide is finite in this case, the quantization of the modes occurs. The eigenvalues of these modes thus become discrete, as marked by black crosses in Figs. 5(b) and 5(c). Obviously, the bigger the radius of the waveguide is, the more eigenmodes exist, because more wavelengths can be fit to the circumference. On the other hand, when the radius becomes smaller than a critical radius R_c, no TPSS mode would occur
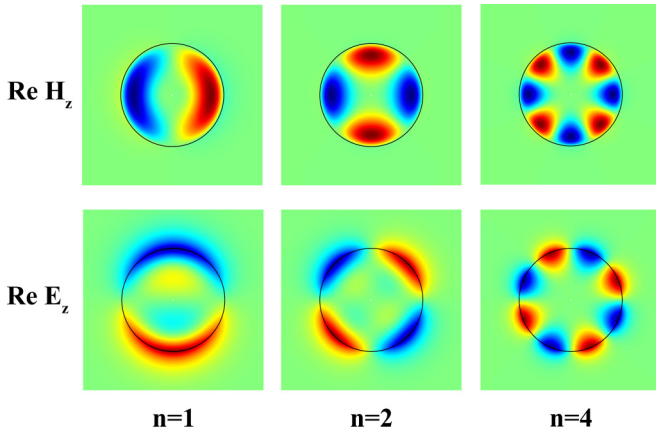
FIG. 6. Distributions of $\mathrm{Re}\,E_z$, $\mathrm{Re}\,H_z$ on the waveguide cross section for $\chi = 0.5$, $k_0 R = 5$, and $n = 1, 2, 4$. These parameters are marked by the blue crosses in Fig. 8.

FIG. 8. Dependence of the wave vector h/k_0 of the eigenmodes of the bianisotropic waveguide on $k_0 R$ for $\varepsilon_d = 1$. Each point denotes a solution of Eq. (10). n is shown by color. Crosses correspond to the parameters for which fields are shown in Figs. 6 and 7.

[see Fig. 5(d) for $k_0 R = 0.5$]. This is because no eigenmode has a wavelength that can cover the circumference.

Strictly speaking, no TPSS are present in the waveguide with a finite radius. This is because with an infinitesimal change of the waveguide radius $R \rightarrow R + \Delta R$, initial longitudinal wave number h is no longer a solution of the dispersion equation and consequently the initial mode disappears through radiation into the environment. This is due to the variations of $\Delta h = h(k_{\varphi 1}) - h(k_{\varphi 2})$ for the neighboring modes. However, in the case of large $k_0 R$ (for $k_0 R \rightarrow \infty$), $\Delta h \rightarrow 0$ and therefore the effect of topologically protection can be observed experimentally because of the finite bandwidth of real signals.

Selected field distributions of TPSS are shown in Fig. 6. One can see that the azimuthal number n corresponds to the number of maxima of the electric and magnetic fields along the circumference of the waveguide. The field distribution along the waveguide (i.e., the z axis) will be discussed in Sec. VIII.

Increasing $k_0 R$ would lead to increasing the number of maxima inside the waveguide. However, since the radial wave vectors q_M and q_P are complex, the fields still decay inside the waveguide. Therefore, to see how the additional maxima appear, let us plot $\arg E_z$ in Fig. 7 for $k_0 R = 2, 4, 8$, which will show clearly the points for which $E_z = 0$ and how a type of the modes appears. Figure 7 shows that increasing $k_0 R$ leads to increasing number of zeros of field inside the waveguide. Note that changing signs of both χ and n preserve values of h.

Now let us study TPSS dependence on $k_0 R$ in more details. Figure 8 shows the dependence of the modes of the

bianisotropic waveguide [i.e., solutions of Eq. (10)] on $k_0 R$ for $\chi = 0.5$ and the environment with $\varepsilon_d = 1$. First of all, one can see from Fig. 8 that all TPSS lie above the $h/k_0 = \sqrt{\varepsilon_d}$ line because below this line radiation losses appear. Second, above the blue dashed line, all eigenmodes are bulk ones inside the bianisotropic cylinder (see also Fig. 4). Thus, the surface modes lie below the blue line. One can see that the modes with the different signs of azimuthal number n have significantly different dependence of $k_0 R$. For a chosen sign of chirality $\chi = 0.5$, the wave vector h/k_0 of the modes with $n < 0$ decrease with decreasing $k_0 R$ (if we do not take into consideration small bends). Moreover, for each n there is a cutoff value for the waveguide radius. In contrast, there is no such cutoff for the modes with $n \geqslant 0$. However, the longitudinal wave vector h/k_0 for these modes increases with decreasing $k_0 R$ and for each mode, there is a critical value of $k_0 R$ below which modes cross the blue line and became bulk high-k hyperbolic modes [25] with large losses, i.e., they disappear as TPSS. Thus, in this section we have shown that for small enough waveguide radius, TPSS do not exist. This means that if the waveguide radius varies along the propagation direction and reaches the critical value at some distance, the TPSS at this point transform into other modes including radiation ones. In other words, at this point full breakdown of the bulk-edge correspondence [30] will occur.

Until this moment all results were obtained from the analytical expressions derived in Sec. II. In the next two sections we use the results of numerical simulations using COMSOL MULTIPHYSICS. To model the chirality we adopt the method described in Ref. [34].
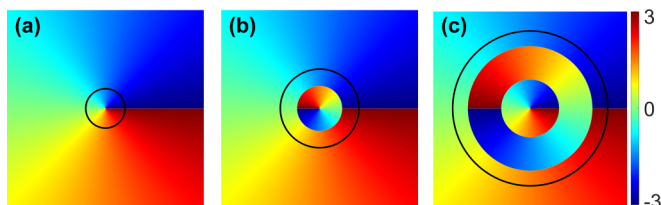

FIG. 7. Distributions of $\arg E_z$ on the waveguide cross section for $\chi = 0.5$, $n = 1$, and $k_0 R = 2, 4, 8$ in (a), (b), and (c), respectively. The parameters used are marked by black crosses in Fig. 8.
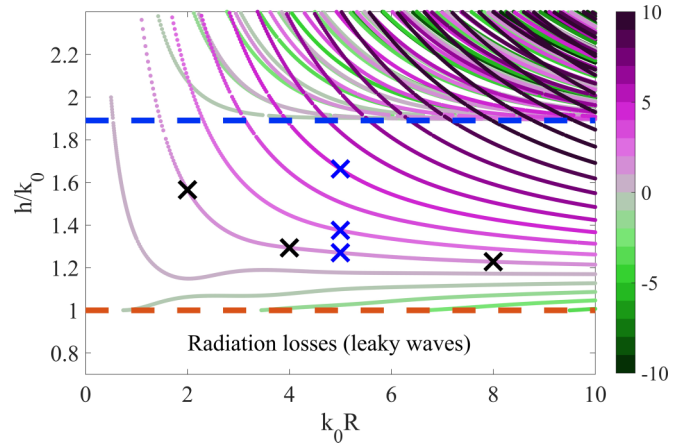
V. TOPOLOGICAL PROTECTED SURFACE STATES ON A TWO-WIRE WAVEGUIDE

As shown in the previous section, TPSS can disappear if the radius of the single-wire waveguide becomes too small. However, it is known from the theory of usual waveguides that varying spatial topology of waveguides can change their cutoff effect substantially. In particular, coaxial and two-wire waveguides have no cutoff at all. Thus, to see how adding
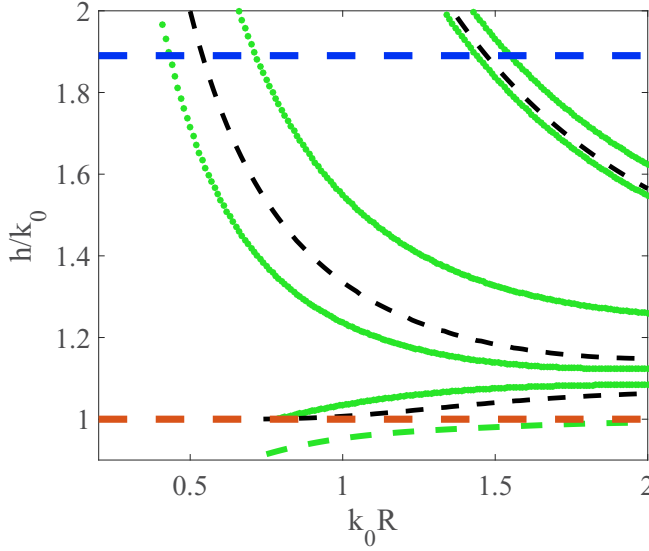
FIG. 9. Wave vector h/k_0 as a function of $k_0 R$ for the two-wire system (green curves). The black dashed lines correspond to the single-wire case (see Fig. 8). The distance between the centers of two cylinders is $2.2R$. Green dashed line corresponds to mode, which is not TPSS.

another wire to the waveguide would affect the TPSS properties, here we study TPSS properties of a two-wire waveguide [see Fig. 1(b)].

In Fig. 9 we plot the h/k_0 as a function of $k_0 R$ for the two-wire waveguide made of bianisotropic materials embedded in the air ($\varepsilon_d = 1$). As usual, modes of two-wire waveguide are symmetric and antisymmetric superpositions of modes of single waveguide. Consequently, the two-wire system has more TPSS modes for $k_0 R < 2$ (e.g., five modes in Fig. 9; the 6th mode is leaky) than the single-wire system (only three modes for $k_0 R < 2$ in Fig. 8). From Fig. 9 one can observe that the curves generally behave like the curves in Fig. 8 (which are shown by dashed black lines). In particular, the cutoff radius $k_0 R_c$ still exists in the two-wire system, although it decreases slightly to $k_0 R_c \approx 0.4$. The existence of the cutoff radius indicates that the limitation of the single-wire system remains unchanged even when another wire is added to the single-wire system. Thus, the results of this section show that two-wire waveguides made of bianisotropic metamaterials with nontrivial topology of reciprocal space have almost the same cutoff effects for TPSS as the single-wire waveguide.

VI. TPSS IN THE WAVEGUIDE WITH A SUPERELLIPTICAL CROSS SECTION

In this section, we will investigate the influence of the shape of the cylinder cross section on the dimensional quantization. In fact, most of the works on topological photonics investigate this effect. Let us consider cylinders with the cross section in a superellipse shape [35] which is defined by equation

$$|x|^N + |y|^N = R_*^N. \tag{14}$$

Eigenmodes of such waveguides with different n values and a fixed perimeter P are displayed in Fig. 10 for $k_0 R = 5$. The fixed perimeter condition is used to keep $k_\varphi P = 2\pi n$ where n
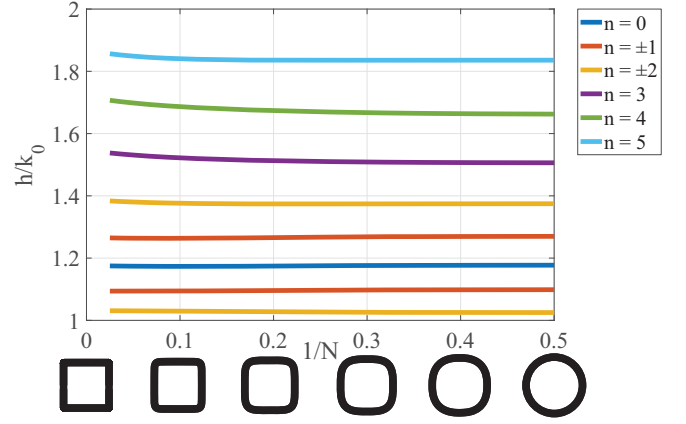

FIG. 10. Longitudinal wave vectors of TPSS modes of a waveguide with a superelliptical cross section with a fixed perimeter [Eq. (14)] for $k_0 R = 5$ as a function of its shape. Bottom row shows the evolution of the cross-section shape from a square to a circle.

is an integer. The value of R_* for each N in Eq. (14) is chosen so that perimeter P remains the same as for a circle of $R = R_*$. Thus, in all cases $P = 2\pi R$. The perimeter of a superellipse can be found from the following formula [35]:

$$P = 4 \sum_{r=0}^{\infty} \sum_{s=0}^{r} \binom{1/2}{r-s} \left(\frac{2(N-1)(r-s)}{N} \right)_s$$
$$\times \frac{1}{s!} \frac{2R_*}{2(N-1)(r-s) + Ns + 1}$$
$$\times 2^{-\{[2(N-1)(r-s)+Ns+1]/N\}}. \tag{15}$$

One can see from Fig. 10 that for large value $k_0 R \gg 1$ the shape has no significant effect on TPSS and the main parameter is the perimeter of the cylinder. This result agrees with results of most of the works on topological photonics.

VII. EFFECT OF THE ENVIRONMENT PERMITTIVITY ON TPSS

Now let us consider how the permittivity ε_d of the host matrix influences TPSS. Mode structures for different ε_d values are shown in Fig. 11 for $k_0 R = 20$ and $\chi = 0.5$. Analysis of Fig. 11 reveals a significant difference between TPSS and edge states in topological insulators. While the edge states are determined exclusively by the topology in the wave-vector space of the bulk topological insulator, TPSS depend significantly on the permittivity of the host medium with trivial topology of isofrequency surfaces. In the case of

$$\varepsilon_d < (\sqrt{\varepsilon_\rho \mu} - |\chi|)^2, \tag{16}$$

TPSS arc connects the regions of equifrequency surfaces of the bulk bianisotropic material with different Chern numbers [Fig. 11(a), $\varepsilon_d = 0.5$]. This situation is similar to topological insulators. In the case of

$$\varepsilon_d > (\sqrt{\varepsilon_\rho \mu} - |\chi|)^2, \tag{17}$$

TPSS arc starts from the equifrequency surface of the trivial host medium and ends at the equifrequency surface of the bianisotropic material with Chern index $C = 1$ [Fig. 11(b),
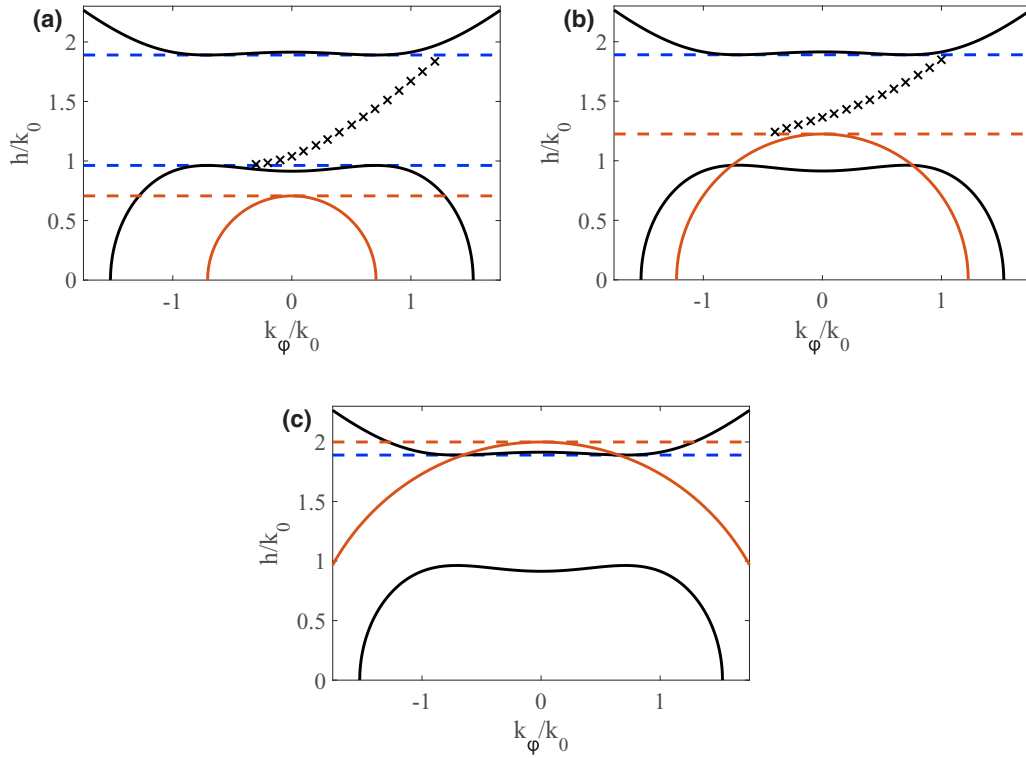
FIG. 11. Eigenvalues [solutions of Eq. (10)] of the bianisotropic waveguide with $k_0R = 20$ and with different values of ε_d (crosses). (a) $\varepsilon_d = 0.5$, (b) $\varepsilon_d = 1.5$, and (c) $\varepsilon_d = 4$. Red semicircles represent the equifrequency surface of the environment.

$\varepsilon_d = 1.5$]. Strictly speaking, in both (a) and (b) cases, TPSS arcs are limited from the top by blue line $b = 0$ (see also Fig. 4). Above this line, eigenmodes of the waveguide become the bulk high-k hyperbolic ones. Finally, when the equifrequency surface of the host medium crosses the top branch of the bianisotropic material, i.e., for $\varepsilon_d > (\sqrt{\varepsilon_\rho \mu} + |\chi|)^2$, there is no TPSS at all [Fig. 11(c), $\varepsilon_d = 4$]. It is important to note that all these conditions are independent of the geometry of the waveguide.

VIII. NEGATIVE REFRACTION OF TPSS

An important property of TPSS of the waveguide is one-way propagation along the φ direction. Usually such propagation is related to the phase velocity. However, from the physical point of view, the group velocity is more important because it is related to the energy flow. Thus, in this section we present the results of our study on how the directions of phase and group velocities of TPSS depend on the parameters of the bianisotropic waveguide.

The direction of phase velocity coincides with the direction of wave vector **k** which is orthogonal to the phase front of the electromagnetic field. For dependence

$$E_z \sim \exp\left(i(hz + n\varphi - \omega t)\right) = \exp(i(hz + k_\varphi l - \omega t)),$$
$$(18)$$

where $l = \varphi R$ is the distance along the circumference, one can see that $\mathbf{k} = \{0, n/R, h\}$. To characterize the direction of group velocity, one should use Poynting vector $\mathbf{S} = c[\mathbf{E} \times \mathbf{H}]/(4\pi)$ with coordinates $\mathbf{S} = \{S_r, S_\varphi, S_z\}$ in the cylindrical coordinate system. It can be shown that for TPSS, $S_r = 0$, S_z, and S_φ do not depend on φ coordinate. Streamlines of Poynting vector and

phase velocity are shown in Fig. 12 for $k_0R = 5$, $k_0R = 1.5$, and $n = -1, 0, 1$.

Figure 12 shows that streamlines of phase velocity have simple behavior, i.e., they change their direction (spirality) together with azimuthal number n. On the contrary, directions
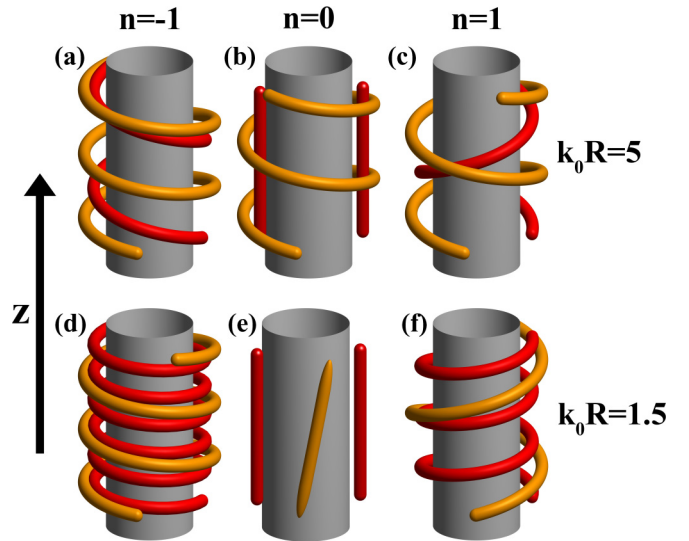

FIG. 12. Streamlines of Poynting vector (orange lines) and phase velocity (red lines) of TPSS with $n = -1$(a), (d), $n = 0$ (b), (e), $n = 1$ (c), (f) for $k_0R = 5$(a)–(c), $k_0R = 1.5$ (d)–(f), and $\chi = 0.5$. The field distribution and Poynting vector are calculated at $\sqrt{x^2 + y^2} = 1.01R$. In all cases the z component of the velocities is in the positive direction of the z axis.
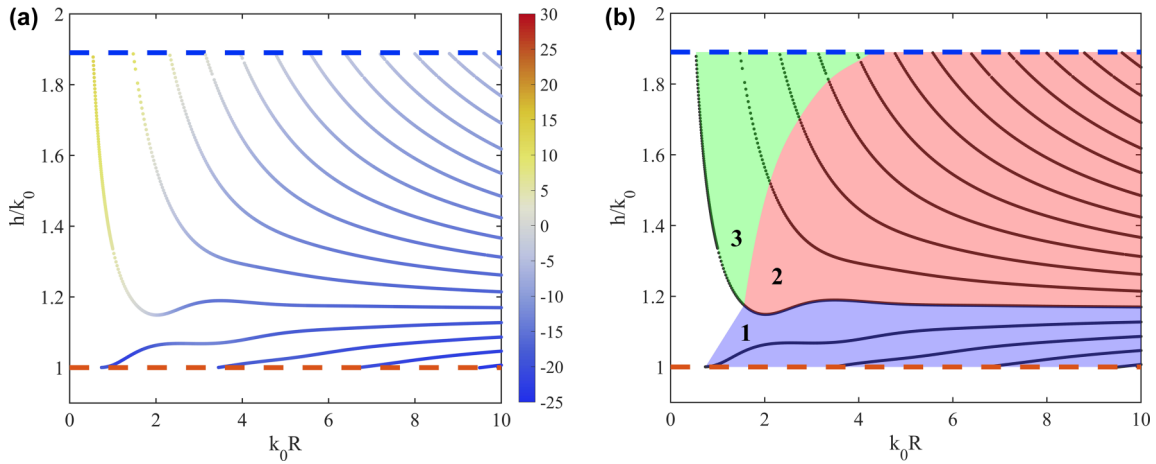
FIG. 13. (a) Direction of group velocity θ, shown by color, for the eigenmodes of the bi-anisotropic waveguide. (b) Three regions of different behavior of phase and group velocities of the eigenmodes. 1-blue region: $v_{ph,\varphi} < 0$ and $v_{g,\varphi} < 0$; 2-red region: $v_{ph,\varphi} > 0$ and $v_{g,\varphi} < 0$ and 3-green region: $v_{ph,\varphi} > 0$ and $v_{g,\varphi} > 0$. Only TPSS modes are shown.

of group velocity exhibit a more complicated behavior. One can see from Fig. 12 that for $k_0 R = 1.5$, the streamline of group velocity varies only slightly upon the variation of azimuthal number n from -1 to $+1$, while for $k_0 R = 5$ it varies significantly and even changes its sign. For $k_0 R = 5$ and $n = 1$, group and phase velocities have different signs of φ component, while for $k_0 R = 1.5$ and $n = \pm 1$, they have the same sign. To study this effect in more details, we plot in Fig. 13 group velocity (Poynting vector) directions of all TPSS shown in Fig. 8. To do this, we introduce the angle of group velocity spiral $\theta = \arctan(S_\varphi / S_z)$. Positive and negative values of θ correspond to clockwise and counterclockwise twist of the spiral of Poynting vector [Figs. 12(d) and 12(f), respectively]. The values of θ are also shown in Fig. 13(a) for TPSS by pseudocolors. It can be seen that for the modes with $n \geqslant 0$, angle θ changes its sign when $k_0 R$ decreases. This change of sign could happen in the TPSS region (zone 3 in Fig. 4). For

the chosen optical parameters of the waveguide, it corresponds to the modes with $n = 0, 1, 2, 3, 4$. Therefore, there are values of $k_0 R$ for which one part of the modes would have $\theta < 0$ and the other part $\theta > 0$. An example of such behavior is shown in Fig. 14 for $k_0 R = 5$. Color of each cross shows a particular region the mode belongs to. Modes with $n = 0$ are shown by black color since they lie on the border of two regions.

As mentioned above, the sign of the φ component of phase velocity $\mathbf{v}_{ph}$ is determined by the sign of n [see Eq. (18)]. On the other hand, the φ component of group velocity $\mathbf{v}_g$ coincides with $\mathbf{S}_\varphi$ and therefore its sign is determined by the sign of θ. If one considers the relative direction of the φ component of phase and group velocities (which define the twist of the spiral) three different regions can be defined [see Fig. 13(b)]. First, for $n < 0$ we have $v_{ph,\varphi} < 0$ and $v_{g,\varphi} < 0$ [region 1—blue color in Fig. 13(b)]. Second, for $n > 0$ and $\theta < 0$ we have $v_{ph,\varphi} > 0$
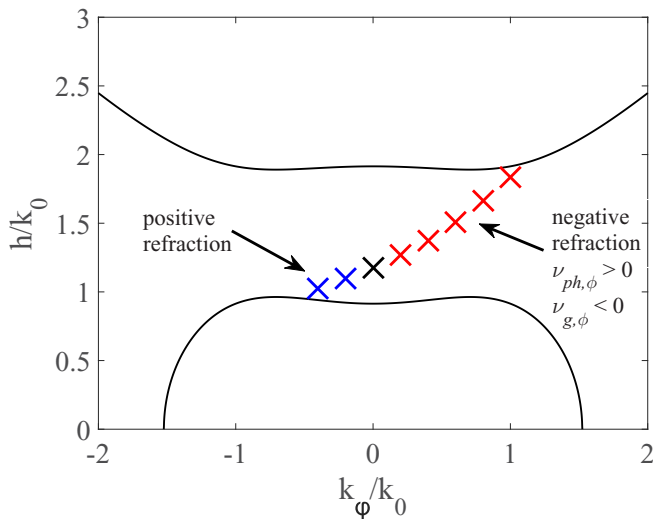

FIG. 14. Eigenvalues (crosses) of the bianisotropic anisotropic waveguide for $k_0 R = 5$. Colors of the crosses indicate the regions in Fig. 13(b) to which the modes belong. Solid lines show bulk equifrequency surfaces.
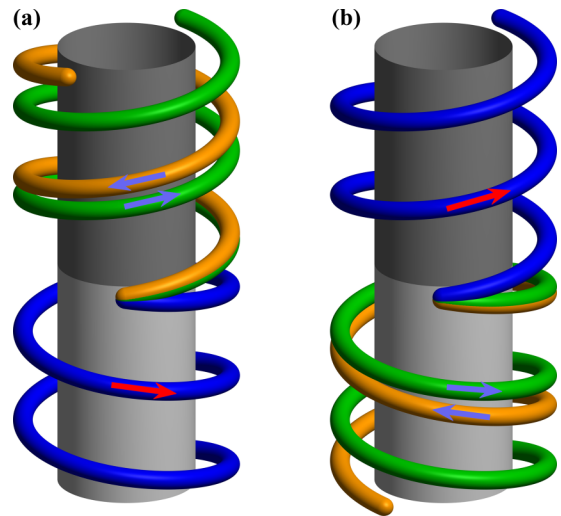

FIG. 15. Light reflection and transmission (Poynting vectors) in TPSS along the interface between two waveguides with different χ values (bottom and top cylinders have $\chi = 0.5$ and $\chi = -0.5$, respectively). The incoming wave is shown by orange color, entering from top in (a) but from bottom (b), while the reflected and transmitted waves are shown by green and blue color, respectively.
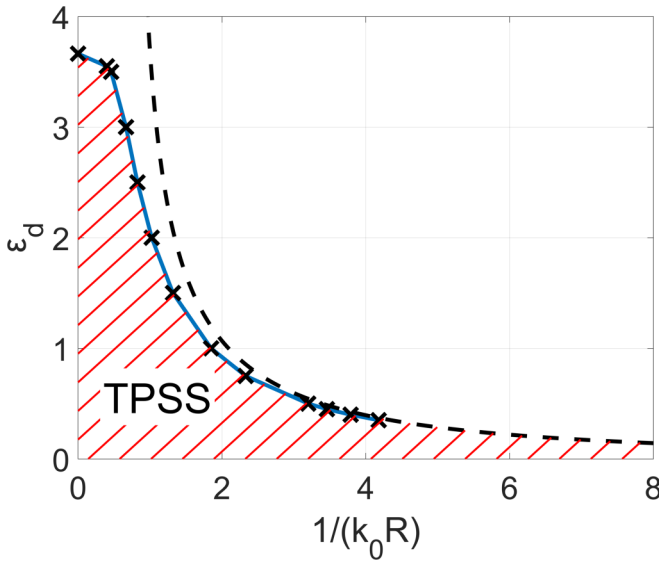
FIG. 16. Phase diagram of TPSS in cylindrical bianisotropic waveguides in coordinates ε_d and $1/k_0R$. Crosses represent the numerical solutions, while the dashed line denotes the asymptotic analytic solution of Eq. (10).

and $v_{g,\varphi} < 0$ [region 2—red color in Fig. 13(b)]. Third, for $n > 0$ and $\theta > 0$ we have $v_{ph,\varphi} > 0$ and $v_{g,\varphi} > 0$ [region 3— green color in Fig. 13(b)]. Thus, in region 2 we have a negative refractive index along the φ direction. Existence of negative refraction for TPSS will result in many interesting effects [37–43]. From Fig. 15 one can see that negative refraction takes place indeed. In particular, in the case of excitation of TPSS with a point source one can expect superlens effect [36–43].

IX. CONCLUSIONS

We have investigated the optical properties of bianisotropic waveguides with nontrivial topological structure in momentum

space surrounded by an ordinary dielectric matrix. In particular, we have derived the exact analytical solution of eigenmodes for the system in the entire parameter space. Our results reveal that the concept of TPSS has only a limited region of applicability in the parameter space. For example, outside this applicable region such as too small radius of the waveguide, TPSS disappear due to the dimensional quantization of the wave vector. Moreover, permittivity ε_d of host dielectric matrix is also found to have significant impact on the structure of TPSS, and TPSS could even disappear when ε_d becomes sufficiently large. This effect is absent in the case of topological insulators, where the existence of edge states depends only on the topological structure of the band zones rather than on topology of the environment. The critical value of the waveguide radius below which TPSS vanish is also shown to depend on the ε_d value. Based on the analytic solution, we have constructed a TPSS phase diagram in space ε_d and $1/k_0R$, as shown in Fig. 16.

We also have studied phase and group velocities of TPSS, and discover that in certain parameter regions, phase and group velocities of TPSS have opposite signs, i.e., TPSS have a negative refractive index. Our interesting findings would be important for designing optical interconnects [22,23] based on waveguides with nontrivial topological structure in momentum space.

[1] R. M. Kaufmann, D. Li, and B. Wehefritz-Kaufmann, Notes on topological insulators, Rev. Math. Phys. **28**, 1630003 (2016).

[2] W. Xiao-Guang, Electron-elastic-wave interaction in a two-dimensional topological Insulator, Chin. Phys. Lett. **33**, 027303 (2016).

[3] V. V. Enaldiev, I. V. Zagorodnve, and V. A. Volkov, Boundary conditions and surface state spectra in topological insulators, JETP Lett. **101**, 89 (2015).

[4] F. Zhang, C. L. Kane, and E. J. Mele, Surface states of topological insulators, Phys. Rev. B **86**, 081303 (2012).

[5] S. Chang, Foundational theories in topological physics garner Nobel Prize, Phys. Today **69**(12), 14 (2016).

[6] L. Lu, J. D. Joannopoulos, and M. Soljačić, Topological photonics, Nat. Photonics **8**, 821 (2014).

[7] W. Gao, M. Lawrence, B. Yang, F. Liu, F. Fang, B. Beri, J. Li, and S. Zhang, Topological Photonic Phase in Chiral Hyperbolic Metamaterials, Phys. Rev. Lett. **114**, 037402 (2015).

[8] A. B. Khanikaev, S. Hossein Mousavi, W. K. Tse, M. Kargarian, A. H. MacDonald, and G. Shvets, Photonic topological insulators, Nat. Mater. **12**, 233 (2013).

[9] L. B. Felsen and N. Marcuvitz, *Radiation and Scattering of Waves* (Wiley-IEEE, New York, 2011).

[10] B. Yang, M. Lawrence, W. Gao, Q. Guo, and S. Zhang, One-way helical electromagnetic wave propagation supported by magnetized plasma, Sci. Rep. **6**, 21461 (2016).

[11] C. W. Hsu, B. Zhen, J. Lee, S. L. Chua, S. G. Johnson, J. D. Joannopoulos, and M. Solijacic, Observation of trapped light within the radiation continuum, Nature (London) **499**, 188 (2013).

[12] D. A. Jacobs, A. E. Miroshnichenko, A. E. Kivshar, and A. B. Khanikaev, Photonic topological Chern insulator based on tellegen metacrystals, New J. Phys. **17**, 125015 (2015).

[13] A. Slobozhanyuk, S. H. Mousavi, X. Ni, D. Smirnova, Y. S. Kivshar, and A. B. Khanikaev, Three-dimensional all-dielectric photonic topological insulator, Nat. Photonics **11**, 130 (2016).

[14] Y. Kivshar and M. Rybin, Optical physics: Anisotropy enables unusual waves, Nat. Photonics **11**, 212 (2017).

[15] H.-C. Chan and G.-Y. Guo, Tuning topological phase transitions in hexagonal photonic lattices made of triangular rods, Phys. Rev. B **97**, 045422 (2018).

[16] Z. Wang, Y. Chong, J. D. Joannopoulos, and M. Soljačić, Observation of unidirectional backscattering-immune topological electromagnetic states, Nature (London) **461**, 772 (2009).

[17] X. Cheng, C. Jouvaud, S. H. Mousavi, A. Z. Genack, and A. B. Khanikaev, Robust reconfigurable electromagnetic pathways within a photonic topological insulator, Nat. Mater. **15**, 542 (2016).

[18] S. Mittal, J. Fan, S. Faez, A. Migdall, J. M. Taylor, and M. Hafezi, Topologically Robust Transport of Photons in a Synthetic Gauge Field, Phys. Rev. Lett. **113**, 087403 (2014).

[19] M. C. Rechtsman, J. M. Zeuner, Y. Plotnik, Y. Lumer, D. Podolsky, F. Dreisow, S. Nolte, M. Segev, and A. Szameit, Photonic Floquet topological insulators, Nature (London) **496**, 196 (2013).

[20] P. Kabos and V. S. Stalmachov, *Magnetostatic Waves and Their Application* (Springer Science+Business Media, Dordrecht, 1994).

[21] A. V. Vashkovskii, A. V. Stalmakhov, and D. G. Shakhnazaryan, Formation, reflection, and refraction of magnetostatic waves beams, Soviet Phys. J. **31**, 908 (1988).

[22] D. A. B. Miller, Optical interconnects to electronic chips, Appl. Opt. **49**, F59 (2010).

[23] C. Sun *et al.*, Single-chip microprocessor that communicates directly using light, Nature (London) **528**, 534 (2015).

[24] I. V. Lindell, A. H. Sihvola, S. A. Tretyakov, and A. J. Viitanen, *Electromagnetic Waves in Bi-anisotropic and Bi-isotropic Media* (Artech House, Boston, 1994).

[25] A. Poddubny, I. Iorsh, P. Belov, and Y. Kivshar, Hyperbolic metamaterials, Nat. Photonics **7**, 948 (2013).

[26] *Handbook of Mathematical Functions*, edited by M. Abramowitz and I. A. Stegun (Dover, New York, 1979).

[27] J. A. Stratton, *Electromagnetic Theory* (McGraw-Hill, New York, 1941).

[28] I. V. Lindell and A. J. Viitanen, Eigenwaves in the general uniaxial bi-anisotropic medium with symmetric parameter dyadic, PIERS **9**, 1 (1994).

[29] M. G. Silveirinha, Chern invariants for continuous media, Phys. Rev. B **92**, 125153 (2015).

[30] M. G. Silveirinha, Bulk-edge correspondence for topological photonic continua, Phys. Rev. B **94**, 205105 (2016).

[31] T. Fukui, Y. Hatsugai, and H. Suzuki, Chern numbers in discretized Brillouin Zone: Efficient method of computing (spin) Hall conductances, J. Phys. Soc. Jpn. **74**, 1674 (2005).

[32] J. F. Dong and J. Li, Characteristics of guided modes in uniaxial chiral circular waveguide, PIERS **124**, 331 (2012).

[33] D. Marcuse, *Theory of Dielectric Optical Waveguides* (Academic, New York, 2012).

[34] V. V. Klimov, I. V. Zabkov, A. A. Pavlov, and D. V. Guzatov, Eigen oscillations of a chiral sphere and their influence on radiation of chiral molecules, Opt. Express **22**, 18564 (2014).

[35] http://www.fractional-calculus.com/super_ellipse.pdf.

[36] V. G. Veselago, The electrodynamics of substances with simultaneously negative values of ε and μ, Sov. Phys. Usp. **10**, 509 (1968).

[37] J. B. Pendry, Negative Refractive Makes a Perfect Lens, Phys. Rev. Lett. **85**, 3966 (2000).

[38] N. Fang, H. Lee, C. Sun, and X. Zhang, Sub-diffraction-limited optical imaging with a silver superlens, Science **308**, 534 (2005).

[39] Z. Liu, H. Lee, Y. Xiong, C. Sun, and X. Zhang, Far-field optical hyperlens magnifying sub-diffraction-limited objects, Science **315**, 1686 (2007).

[40] I. I. Smolyaninov, Y.-J. Hung, and C. C. Davis, Magnifying superlens in the visible frequency range, Science **315**, 1699 (2007).

[41] V. Klimov, Novel approach to a perfect lens, JETP Lett. **89**, 229 (2009).

[42] V. Klimov, S. Sun, and G.-Y. Guo, Coherent perfect nanoabsorbers based on negative refraction, Opt. Express **20**, 13071 (2012).

[43] D. V. Guzatov, and V. V. Klimov, Focusing of dipole radiation by a negative index chiral layer 2. A thin layer as compared with the wavelength, Quantum Electron. **44**, 1112 (2014).